Defect Detection in Bidirectional Glass Fabric Reinforced Thermoplastics Based on 3-D-THz Imaging

Aya Souliman, Matthias Kahl, Daniel Stock, Michael Möller, Bernd Engel, and Peter Haring Bolívar

***Abstract*—Nonhomogeneous, bidirectional glass fabric reinforced thermoplastic (GFRT) composites are used in the automobile industry to produce economic and environment friendly vehicles. Despite the fact that GFRT materials have superior mechanical characteristics and lower manufacturing cost compared with traditional materials, they are prone to significant deformation and defect emergence during the forming/manufacturing of parts from prefabricated laminates. Some defects, especially hidden ones like delamination and consolidation defects, can significantly reduce the mechanical properties of the final parts. It is essential to use 3-D nondestructive testing technology to detect and identify such hidden defects. This research investigates the ability of 3-D-THz imaging to detect hidden defects (i.e., delamination and consolidation) in GFRT composite materials. Frequency modulated continuous wave (FMCW) technique is used to generate 3-D-THz cross-sectional images. Nondefective and defective samples with a thickness of 1.5 mm have been measured with two 3-D THz imaging systems operating in the frequency range from 238 to 316 GHz and from 499 to 733 GHz. In addition, a simulation of the reflected FMCW spectrum is presented to analyze the measurements and intercompare the performance of the two imaging systems. A systematic analysis in a large sample set demonstrates that a delamination defect with a thickness of 125 μm as well as a consolidation defect with a difference in thickness less than 0.4 mm can be successfully detected by the 700-GHz imaging system.**

***Index Terms*—3-D-THz imaging, composite materials, defect detection, frequency modulated continuous wave (FMCW), glass fabric reinforced thermoplastic (GFRT), nondestructive testing (NDT), terahertz (THz).**

I. Introduction

LIGHTWEIGHT composite materials are increasingly witnessing a great focus from researchers and industries in different sectors like building and construction, transportation, robotics, and mechanical engineering [1], [2], [3], and [4].

Fiber reinforced polymers (FRP) are lightweight composite materials consisting of many layers of fibers encased in polymer matrices [5]. The FRP composites have diverse forms based on the type of fiber and the category of polymer. Each of them has several mechanical properties and is adequate for a specific application area [6], [7]. In the automotive industry, the glass fiber reinforced thermoplastic (GFRT) is intensely envisaged as an attractive new alternative to produce vehicle parts. This is not only due to the low-cost processing of the parts by conventional forming procedures in presses but also due to the high stiffness, low weight, corrosion resistance, and recyclability in comparison to traditional materials, such as iron, copper, and steel [8], [9]. However, during the production of the GFRT panels (semifinished products), the fibers can be displaced, damaged, or torn. Besides, any insufficient temperature, pressure, or cooling can cause a layers separation or a difference in the material thickness. Moreover, during forming the finished parts, additional defective areas can be created or existing defects can be enlarged [10]. As such materials are starting to be used in mechanically relevant parts of cars, any deformation in the material or deficiency in the fiber distribution decreases material's stiffness and strength that, hence, affects the car safety. For that reason, nondestructive testing (NDT) is crucial to detect outer and/or inner distortions in such materials without causing damage to the original part.

Various NDT techniques are available, such as visual, ultrasound, infrared thermography, and X-ray testing, and each has strengths and shortcomings [11]. For example, the visual inspection is widely used to detect defects in the surface due to its simplicity and reliability, but it is not sufficient for hidden defect detection. The X-ray technology can provide a high resolution 3-D-image with an accurate position of hidden defects, but, unfortunately, it ionizes molecules. For this reason, it requires shielding which makes it impractical for direct use in manufacturing lines in factories. The ultrasonic testing (UT) is a safe solution, but it is not suitable to inspect thin, rough, or heterogeneous materials. The infrared thermography (IRT) is a safe, low-energy measurement system that can be used easily for in-line inspection, but cannot provide information about the defect position in depth.

Manuscript received 29 April 2022; revised 13 November 2022 and 29 December 2022; accepted 4 February 2023. Date of publication 22 February 2023; date of current version 3 May 2023. This work was supported by the Federal Ministry of Education and Research (BMBF) under Grant 13N14632 [Adaptive Multimodal in-line Inspection of fiber-reinforced Thermoplastics for automotive lightweight construction (AMITIÉ) Project]. *(Corresponding author: Aya Souliman.)*

Aya Souliman, Matthias Kahl, Daniel Stock, and Peter Haring Bolívar are with the Institute for High Frequency and Quantum Electronics, University of Siegen, 57076 Siegen, Germany (e-mail: aya.souliman@uni-siegen.de; matthias.kahl@uni-siegen.de; daniel.stock@uni-siegen.de; peter.haring@uni-siegen.de).

Michael Möller is with the Computer Vision Group, University of Siegen, 57076 Siegen, Germany (e-mail: michael.moeller@uni-siegen.de).

Bernd Engel is with the Institute of Forming Technology, University of Siegen, 57076 Siegen, Germany (e-mail: Bernd.Engel@uni-siegen.de).

Color versions of one or more figures in this article are available at https://doi.org/10.1109/TTHZ.2023.3247609.

Digital Object Identifier 10.1109/TTHZ.2023.3247609

Imaging at terahertz frequencies offers an interesting direct 3-D subsurface imaging capability without requiring ionizing radiation.

The main weakness of the THz image compared to the X-ray and optical ones is the lower resolution. Nevertheless, due to the great advances of THz technology, recently the enhancement of the THz image resolution has been given a great focus by researchers either by improving the THz imaging techniques [12], [13], [14], [15] or developing super resolution algorithms [16], [17], [18], [19], [20].

The rest of this article is organized as follows. In Section II, prior research in the field of NDT of composite materials based on THz technologies are summarized. In Section III, the measured samples and the THz-FMCW imaging system are explained. Furthermore, the THz-FMCW reflected signal is simulated. The measurement results of 300 and 700-GHz imaging systems are presented and discussed in detail throughout Section IV. Finally, Section V concludes this article.

II. State of the Art

In the field of composite materials inspection based on THz technologies, most prior research implemented terahertz time domain spectroscopy (THz-TDS) systems to detect different kinds of defects in various types of composite materials like carbon fiber reinforced polymer (CFRP) [21], [22], [23], [24] and glass fiber reinforced polymer (GFRP).

The inspected GFRP composites have different kinds of polymer like plastic (glass fiber prepreg) [25], [26], polyimide resin [27], polyamide and ultramid [28], and epoxy resin [29]. However, the thermoplastics composites, which have different characteristics than other polymer composites, have not been studied in detail yet.

The THz-TDS is a broadband system (up to 10-THz bandwidth) based on femtosecond lasers to generate THz-pulses; therefore, it is a good choice to inspect thin composite materials and measure thicknesses in the μm range. For example, in [25] multidelamination defects in a commercial unidirectional glass fiber reinforced plastic composite material with a thickness of 1.5 mm have been detected based on the THz-TDS imaging system with a frequency range from 0.1 to 3 THz. The delamination layers have been produced by inserting Teflon films with a thickness of 100 μm between the GFRP layers. Although the THz-TDS is not a 3-D imaging system, the authors could successfully determine the location of each delamination in Z-direction as well as calculate the thickness of each one by analyzing the THz-waveforms in the time-domain.

Since the composite materials have to be inspected in-line; as a consequence, the researchers in this field have recently focused more on the THz systems based on all-electronic devices in spite of the comparatively lower bandwidth (in the GHz range) of those systems. The THz-FMCW is a narrow-band low-power system based on all-electronic devices to generate a continuous frequency. This technique gives information about the Z-direction in the frequency domain and by moving the system along X and Y directions, a 3-D-image can be measured easily. Although this system has some limitations in both depth and lateral resolutions, some researches have shown promising results in detecting defects in the composite materials based on this system. For instance, Becker et al., [30] reported some results about detecting a delamination defect in the oxide fiber reinforced ceramic composites with two different thicknesses of 10 and 3 mm using the THz-FMCW system running at 100 and 300 GHz, respectively. In [31], a hole defect has been detected, but, in a homogeneous material [polytetrafluoroethylene (PTFE)] with a thickness of 1.5 cm based on FMCW THz radar with an operation frequency of 100 GHz and a bandwidth of 35 GHz.

However, to speed up the scanning time of the single-transmitter–single-receiver THz-FMCW 3-D-imaging system, currently we and many more researchers are working on expanding such systems to high-speed multiple-input–multiple-output (MIMO) imaging system [12], [13] in order to reach real-time imaging capabilities. In [32], the authors have designed a THz system with six sensors (three receivers facing three transceivers) based on the FMCW technology and the system has been tested on a glass fiber reinforced plastics material with different thicknesses of 5, 6, 7, and 10 mm.

In previous research, up to our knowledge, THz-FMCW systems have been basically used to detect defects in materials with thicknesses higher than 3 mm due to the depth resolution limitation. In addition, none of the previous researches (neither those based on the THz-TDS nor the THz-FMCW) have inspected the GFRP composites in which the thermoplastic material is used as polymer matrices [glass fiber reinforced thermoplastic (GFRT)]. Our main contribution is to build high-bandwidth all-electronic 3-D-THz imaging system to detect subsurface defects for the first time in a thin (1.5-mm thickness), inhomogeneous, bidirectional E-glass fiber reinforced thermoplastic composite material. A detailed description and introduction to our system is presented in [33], [34], [35], and [36].

III. Experimental

A. Inspected GFRT Laminates

The analyzed samples are made from a bidirectional twill 2/2 E-glass roving fiber reinforced polypropylene. The twill 2/2 indicates that two wrap yarns (the horizontal fibers) travel over and under two weft yarns (the vertical fibers) that performs a diagonal pattern which is seen in the photograph of the nondefective sample in Fig. 4(g). E-glass is a type of the glass fiber that has low electrical conductivity. Polypropylene is a thermoplastic material which softens at a temperature from 160 to 208 °C [37] and hardens again when it is cooled down. This property gives the GFRT composite material the ability to be reshaped and recycled [38].

In general, the semifinished product of the GFRT composite material is produced by layering the glass fabric and the thermoplastic plies then applying a glass-transition temperature and a certain pressure to combine them. After that, the compressed layers are cooled down [38], [39], [40], [41]. However, any inadequacy in the temperature, pressure, or cooling can lead to different sorts of distortions.

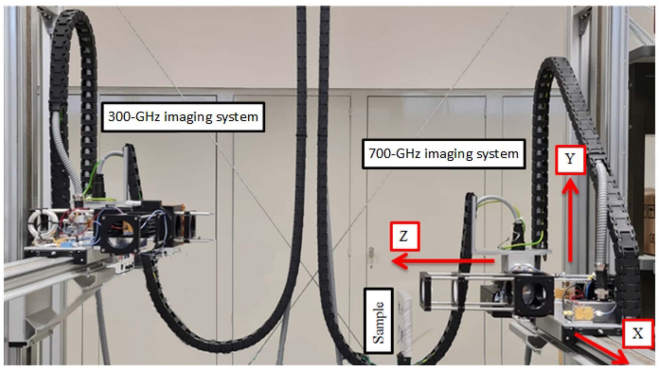

Fig. 1. 3-D-THz imaging systems platform. Left: 300-GHz imaging system with a bandwidth of 78.17 GHz. Right: 700-GHz imaging system with a bandwidth of 234 GHz. Middle: Sample holder.

The inspected specimens consist of three layers, i.e., two outside layers and one middle layer. They have dimensions of 80*25 mm with a thickness between 1.3 to 1.5 mm. In this research, three different specimens of GFRT laminates have been measured as follows.

1) Nondefective specimens.
2) *Defective Specimens With a Delamination Defect:* the delamination defect can be defined as a separation in layers. It is considered the most critical defect in GFRT laminates [10], [42], [43], [44]. It has been produced in this project by inserting a kapton film with a thickness of 125 μm to separate the sample layers.
3) *Defective Specimens With a Consolidation Defect:* the consolidation defect is a variation in the specimen thickness. It happens due to the implementation of low/insufficient pressure during the incorporation of the GFRT layers. This causes the layers of the fabric to rise up, creating holes which are subsequently filled with the melted thermoplastics.

B. 3-D THz Imaging Setup

In this project, two all-electronic 3-D-THz imaging systems with identical configuration but different operation frequencies and bandwidths have been built to examine the effect of the frequency and bandwidth on a defect detection in GFRT laminates.

Fig. 1 shows the platform of the 300 and 700-GHz imaging systems. The two 3-D imaging systems are based on the FMCW technology [45], [46], [47], [48], [49], [50], [51], [52], [53], [54], [55], [56], [57] and they are similar to the system in [33] and [34]. The imaging unit in both systems consists of a hollow wave guide transmitter and receiver mounted on the same platform. The 2-D image is generated by driving the imaging unit (transceiver) along the *X* and *Y* directions using two stepper motors with a step size of 0.2625 mm. The sawtooth FMCW signal is continuously transmitted to measure along the *Z*-direction. At each lateral position the depth is measured and by scanning the entire sample, the cross-section images are generated.

Table I presents the system parameters. The 300-GHz imaging system operates within the frequency range from 238.73 to 316.9 GHz and a bandwidth of 78.17 GHz, whereas the frequency range of the 700-GHz imaging system is from 499 to 733 GHz and the bandwidth is 234 GHz.

TABLE I
3-D THz-FMCW Systems Parameters

Parameter	Symbol	300-GHz imaging system	700-GHz imaging system	Unit
Operation frequency	F_0	277.8173	616	GHz
Start frequency	F_s	238.7308	499	GHz
End frequency	F_e	316.9038	733	GHz
Bandwidth	B	78.1730	234	GHz
Imaging distance	R_0	41.4	38	mm
Lens diameter	D	2	2	inch
Lateral resolution	$\delta_{x,y}$	1	0.4454	mm
Depth resolution in air	$\delta_{Z_{\text{air}}}$	1.9	0.64	mm

TABLE II
Measured Refractive Index and Depth Resolution

	300-GHz imaging system	700-GHz imaging system	Unit
$\underline{n}_{\text{GFRT}}$	2.76 - 0.039i	2.39 - 0.06i	
$\delta_{Z_{\text{GFRT}}}$	0.692	0.267	mm
$\underline{n}_{\text{kapton film}}$	1.83 - 0.012i	1.83 - 0.019i	
$\delta_{Z_{\text{kapton film}}}$	1.3	0.35	mm

The lateral resolution is calculated based on (1), where λ is the wave length and N_A is the numerical aperture

$$\delta_{x,y} = \frac{0.61\lambda}{N_A}. \tag{1}$$

The depth resolution is determined by the Rayleigh limit (2), where c_0 is the speed of light, n is the refractive index, and B is the bandwidth

$$\delta_Z = \frac{c_0}{2nB}. \tag{2}$$

The complex refractive indices of the GFRT and kapton film materials have been measured using the transmission mode of the time-domain spectroscopy [58]. Based on (2) and the measured refractive index, the depth resolution in the GFRT and kapton film materials can be calculated. Table II presents the measured complex refractive index and the calculated depth resolution for both materials and both system frequency operation ranges.

C. Simulation of Reflected THz-FMCW Signal

In this section, the mathematical model of the THz reflected signal from a material with a thickness of Δz_1 are derived to help us analyze the real measurements and compare the performance of the two imaging systems. In general, the number of reflections from different mediums equals to

$$N_r = N_m - 1 \tag{3}$$

where

- N_r is the number of reflections;
- N_m is the number of mediums.

Accordingly, the number of reflections from a material in air (air–material–air) is two reflections. Fig. 2 presents the block diagram of the transmission and reflection components of the

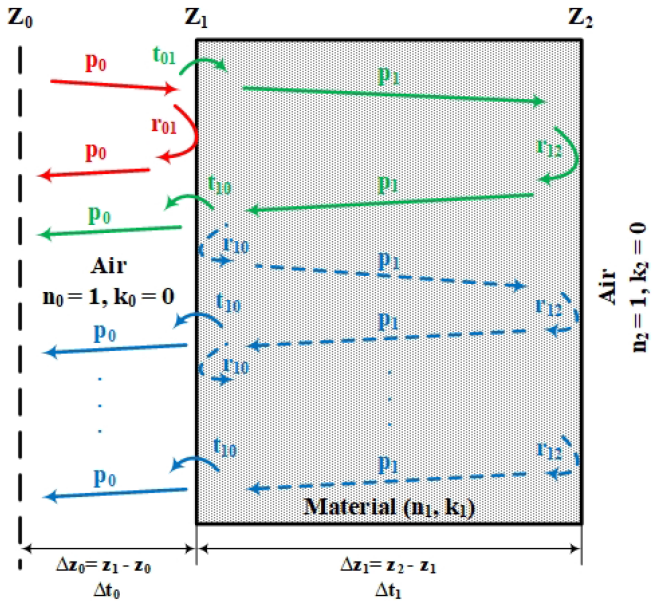

Fig. 2. Block diagram of the transmission and reflection components of the THz-FMCW transmitted signal. Red path presents the reflection from the material surface. Green path is the reflection from the material backside. Dashed blue path states Fabry-Pérot effect.

reflected THz-FMCW signal from a material with a thickness of Δz_1 in air. Z_0 is the reference plane. The ideal reflected signal $\underline{E}_{\text{ideal}}(\omega)$ at an angular frequency ω is given by

$$\underline{E}_{\text{ideal}}(\omega) = E_1(\omega) + E_2(\omega) \cdot \sum_{i=0}^{\infty} [\underline{p}_1^2(\omega, \Delta z_1) \cdot \underline{r}_{12}(\omega) \cdot \underline{r}_{10}(\omega)]^i \tag{4a}$$

$$E_1(\omega) = \underline{p}_0(\omega, \Delta z_0) \cdot \underline{r}_{01}(\omega) \cdot \underline{p}_0(\omega, \Delta z_0) \tag{4b}$$

$$E_2(\omega) = \underline{p}_0(\omega, \Delta z_0) \cdot \underline{t}_{01}(\omega) \cdot \underline{p}_1(\omega, \Delta z_1) \cdot \underline{r}_{12}(\omega) \cdot \underline{p}_1(\omega, \Delta z_1) \cdot \underline{t}_{10}(\omega) \cdot \underline{p}_0(\omega, \Delta z_0) \tag{4c}$$

where E_1 is the reflected signal from the material surface Z_1 and E_2 is the reflected signal from the material backside Z_2. The sum term represents the backward and forward reflections inside the material [Fabry-Pérot effect (FP)] [58]. Since it is a geometric series it can be written as

$$FP(\omega) = \sum_{i=0}^{\infty} [\underline{p}_1^2(\omega, \Delta z_1) \cdot \underline{r}_{12}(\omega) \cdot \underline{r}_{10}(\omega)]^i = \frac{1}{1 - \underline{p}_1^2(\omega, \Delta z_1) \cdot \underline{r}_{12}(\omega) \cdot \underline{r}_{10}(\omega)} \tag{5}$$

where

- $\underline{p}$ is the propagation factor through a medium m with a thickness of Δz_m

$$\underline{p}_m(\omega, \Delta z_m) = e^{-i\frac{\omega \underline{n}_m \Delta z_m}{c_0}} \tag{6}$$

- $\underline{r}$ is the reflection from a medium m when hitting the next medium $m+1$

$$\underline{r}_{m\,m+1}(\omega) = \frac{\underline{n}_m(\omega) - \underline{n}_{m+1}(\omega)}{\underline{n}_m(\omega) + \underline{n}_{m+1}(\omega)} \tag{7}$$

- $\underline{t}$ is the transmission coefficient from a medium m to the next medium $m+1$

$$\underline{t}_{m\,m+1}(\omega) = \frac{2\underline{n}_m(\omega)}{\underline{n}_m(\omega) + \underline{n}_{m+1}(\omega)} \tag{8}$$

- $\underline{n}$ is the complex refractive index of a medium m

$$\underline{n}_m = n_m - k_m i \tag{9}$$

- n_m is the refractive index and k_m is the extinction coefficient of a medium m;
- Δt_m is the time of flight (ToF) in a medium m

$$\Delta t_m = n_m \frac{2\Delta z_m}{c_0}. \tag{10}$$

This quantity is measured around a center function ω_c with a finite bandwidth B. Thus, the overall signal is given by

$$E(\omega) = \underline{E}_{\text{ideal}}(\omega) \cdot \text{rect}\left(\frac{\omega - \omega_c}{2\pi B}\right). \tag{11}$$

Assuming the reflection interfaces of the material are perfectly flat resulting in completely separate reflections ($\underline{p}_1^2(\omega, \Delta z_1) \cdot \underline{r}_{12}(\omega) \cdot \underline{r}_{10}(\omega) \ll 1 \Rightarrow FP(\omega) \cong 1$). By implementing the inverse Fourier transform on (11) and folding by the Dirac signal, the expected reflected signal in the time-domain can be calculated as follows:

$$E(t) = E_1(t) + E_2(t) \tag{12a}$$

$$E_1(t) = E_0 B \text{sinc}(B(t - \Delta t_0)) e^{\omega_c (t - \Delta t_0) i} r_{01} \tag{12b}$$

$$E_2(t) = E_0 B \text{sinc}(B(t - (\Delta t_0 + \Delta t_1))) e^{\omega_c (t - (\Delta t_0 + \Delta t_1)) i} t_{01} r_{12} t_{10} e^{-\alpha_1 \Delta z_1} \tag{12c}$$

where

- E_0 is the initial transmitted signal;
- α_m is a constant equals to

$$\alpha_m = k_m \frac{2\omega_c}{c_0}. \tag{13}$$

From (12a) it can be seen that the expected reflected signal from a material with a thickness of Δz_1 is the summation of two sinc functions $E_1(t)$ (12b) and $E_2(t)$ (12c), which symbolize the reflection from the surface and the backside, respectively. Moreover, the term $e^{-\alpha_1 \Delta z_1}$ in (12c) shows that the amplitude of the second reflection is inversely proportional to the material extinction coefficient k_m and its thickness Δz_1.

The model of the reflected THz-FMCW signal (12) has been simulated in MATLAB. For simplicity, noise is neglected and the reference plane Z_0 is assumed to be on the sample surface ($\Delta z_0 = 0$ mm). The GFRT material with a thickness of $\Delta z_1 = 1.5$ mm has been considered. Fig. 3(a) exhibits the simulated $E_1(t)$ (the blue curve) and $E_2(t)$ (the red curve) of the 300-GHz imaging system and Fig. 3(c) represents their sum. Similarly, Fig. 3(b) and (d) display the simulated signals of

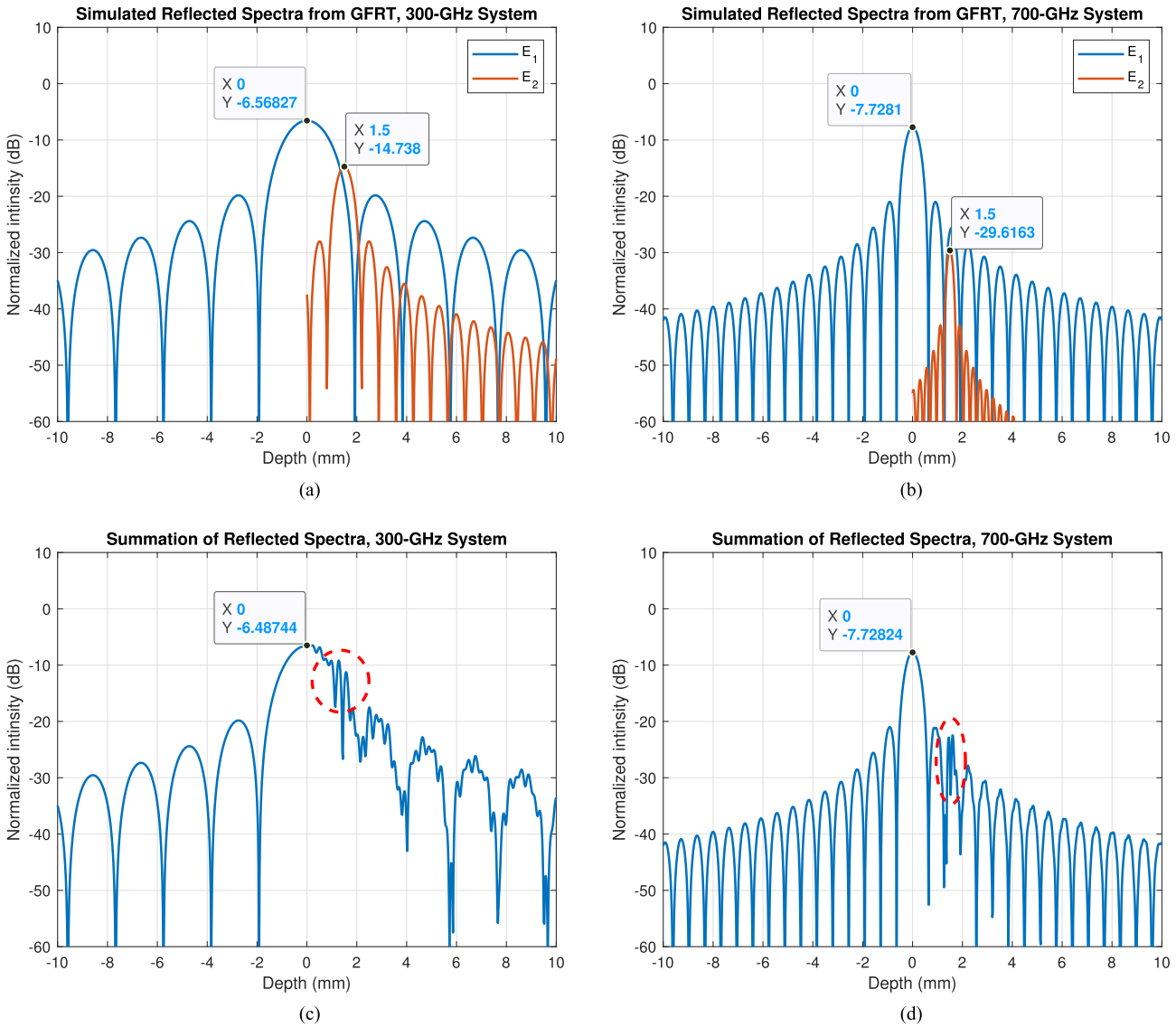

Fig. 3. Comparison of the simulated reflected signals of the 300-GHz imaging system (left) and the 700-GHz imaging system (right) reflected from the GFRT composites with a thickness of $\Delta z_1 = 1.5$ mm in air. (a) and (b) Simulated reflected signal from the front and rear faces of the GFRT material. (c) and (d) Summation of the two reflected signals in (a) and (b), respectively.

the 700-GHz imaging system. It can be clearly observed that the depth resolution of the 700-GHz imaging system has been dramatically improved due to the bandwidth expansion from 78.17 to 234 GHz, which cannot be achieved in the 300-GHz imaging system due to the system limitations. On the other hand, based on the characteristics of the GFRT material (Table II), the extinction coefficient k is larger at higher operation frequency. This will, accordingly, affect the penetration and reduce the amplitude. Please notice from Fig. 3(b) that the difference in amplitude between two reflections in the 700-GHz imaging system is around -21.8 dB, while it is approximately -8 dB in the 300-GHz imaging system in Fig. 3(a).

From Fig. 3(c) and (d) the side-lobes effect on the depth resolution can be clearly seen. For example, in Fig. 3(d) instead of observing the second pick, which presents the reflection from the backside of the material, at depth $= 1.5$ mm two picks appear at depths 1.45 and 1.61 mm. This is due to the summation of the second side-lobe of the reflected spectrum from the front surface with the main pick of the reflection from the backside. However, to suppress the effect of the side-lobes on the depth resolution, Hamming window has been implemented on the measured data.

IV. Results and Discussion

This section presents the experimental results of the defective and nondefective samples measured by the 300 and 700-GHz imaging systems. In addition, a comparison of the results of the two imaging systems is presented.

The specimens have been scanned by placing each one on a low refractive index foam sheet to minimize spurious reflections. The foam sheet is mounted in front of the transceiver unit at a distance R_0 equals to 41.4 mm in the 300-GHz imaging system

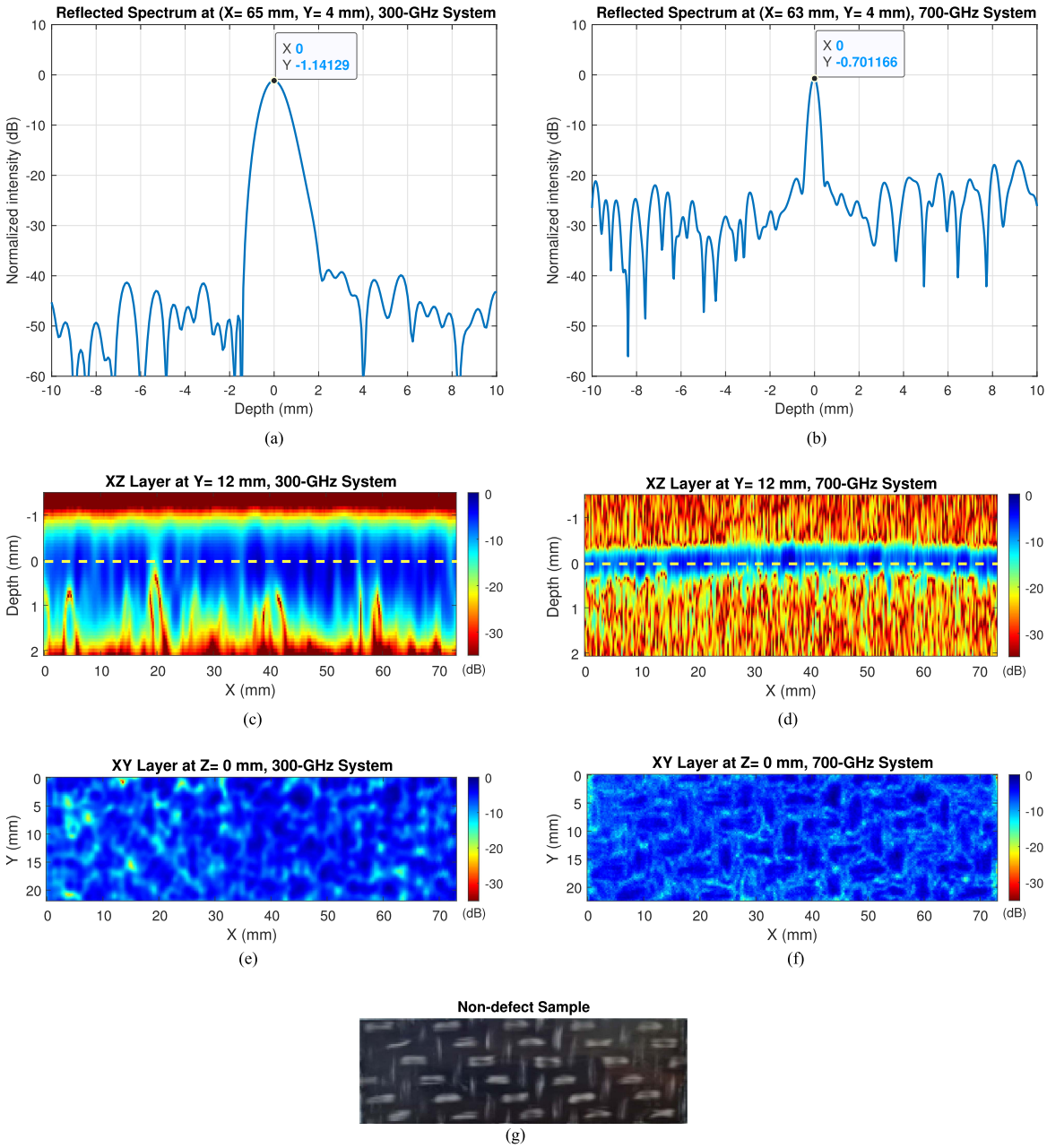

Fig. 4. Comparison of 300-GHz (left) and 700-GHz (right) imaging systems results measured from nondefective sample. (a) and (b) Reflected spectrum from a single point of the measured sample. (c) and (d) Depth layer (*XZ* layer) at $y = 12$ mm. The dashed yellow line in both figures denotes to the surface reflection ($z = 0$ mm). (e) and (f) Amplitude image of the specimen surface (*XY* layer at $z = 0$ mm). (g) Photograph of the measured nondefect sample.

and 38 mm in the 700-GHz imaging system (Table I). Scanning one sample with dimensions of 80*25 mm takes approximately 14 min. During the measurement, each measured point is normalized based on

$$M_{\text{norm}} = \frac{M - M_{\text{min}}}{M_{\text{max}} - M_{\text{min}}} \tag{14}$$

where

- M_{max} is the maximum reflection measured from a metallic target.
- M_{min} is the minimum reflection measured without any target.
- M is the reflection measured from a specimen.

The measurements and data collection are controlled by a LabVIEW program. After data collection, the 3-D-THz images are calculated and plotted in MATLAB by implementing the inverse Fourier transform to the Hamming window of the zero-padded data. The Hamming window and zero-padding have been implemented to suppress side-lobes and smooth out the reflected signals, respectively. It is worth to mention that the maximum signal-to-noise ratio (SNR) in the 300-GHz imaging system is around -35 dB, while the maximum SNR in the 700-GHz imaging system is about -20 dB.

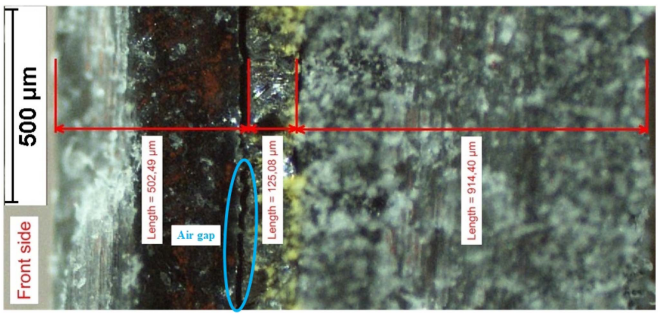

Fig. 5. Microscope image of the *XZ* side of the defective sample with a delamination defect. Yellowish layer is the inserted kapton film. Blue ellipse points to the air-gap.

A. Nondefective Sample

The nondefective sample has been measured by both FMCW imaging systems. Fig. 4 compares the results from both systems, where the left column represents the 300-GHz imaging system results and the right one shows the 700-GHz imaging system results. The photograph of the measured nondefective sample can be seen in Fig. 4(g).

Fig. 4(a) presents the reflected spectrum from the nondefective sample at $x = 65$ mm and $y = 4$ mm measured by the 300-GHz imaging system, while Fig. 4(b) represents the reflected spectrum from the nondefective sample at $x = 63$ mm and $y = 4$ mm measured by the 700-GHz imaging system. From Fig. 4(a) and (b) it can be noticed that the reflected spectrum in both systems has only a single peak which denotes that the reflection from the rear face of the nondefective specimen cannot be distinguished. Looking at the depth layer (*XZ* layer at $y = 12$ mm) in Fig. 4(c) and (d), where the dashed yellow line in both figures refers to the surface reflection, it can be observed that the reason for the inability to distinguish the reflection from the rear face of the GFRT laminates in both systems is given by two different effects.

In the 300-GHz imaging system, the depth resolution in the air $\delta_{Z_{\text{air},300}} = 1.9$ mm is on the order of the sample thickness $\Delta z_1 = 1.5$ mm; hence, the reflection from the backside cannot be separated clearly from the surface reflection. For this reason, in the *XY* amplitude image at $z = 0$ mm in Fig. 4(e), the fiber pattern of the surface cannot be seen obviously because this reflection includes not only the reflection from the front surface but also the reflections from the backside.

In the 700-GHz imaging system, this problem is solved because the depth resolution in the air $\delta_{Z_{\text{air},700}} = 0.64$ mm is significantly smaller than the sample thickness $\Delta z_1 = 1.5$ mm. However, it can be observed from Table II that the extinction coefficient k is higher at higher frequencies ($k_{\text{GFRT},700} = 0.06 > k_{\text{GFRT},300} = 0.039$); therefore, increasing operation frequency inevitably decreases the amplitude of the backside reflection.

From the simulation results, it is expected that the difference in the amplitude between the front and rear interface signals at 616-GHz operation frequency is around -21.8 dB. Taking into account that in the real measurement, the SNR is around -20 dB, this means that the backside reflection cannot be distinguished from noise. In contrast to the 300-GHz imaging system, the *XY* amplitude image at $z = 0$ mm in the 700-GHz imaging system in Fig. 4(f) shows the fiber pattern of the GFRT surface clearly due to the higher depth resolution of the 700-GHz imaging system $\delta_{Z_{\text{GFRT},700}} = 0.267$ mm.

B. Defective Samples: Delamination Defect

To imitate the delamination defect, kapton film with a thickness of 125 μm has been inserted between GFRT layers before applying the glass-transition temperature and pressure. Due to the fact that the kapton film does not melt before +400 °C [59], it will separate the GFRT layers. This separation can be seen in the microscope image of the cross section (*XZ* side) of the defective sample with a delamination defect in Fig. 5, where the yellowish layer shown in Fig. 5 represents the inserted kapton film and the blue ellipse points to the separation. The photograph of the measured defective sample with a delamination defect can be seen in Fig. 6(i).

In order to get a rough idea about the position of the delamination defect in depth, the distance between the front surface of the GFRT specimen and the front face of the kapton film at different points in the microscope image has been measured. It has been found that the delamination position varies between 0.4 to 0.7 mm due to the inhomogeneity of the GFRT composite material.

From (3), the number of expected reflections is four, because the number of mediums are five (Air, GFRT, kapton film, GFRT, Air). However, because the thickness of the kapton film (125 μm) is less than the depth resolution in the kapton film in both systems $\delta_{Z_{\text{kapton-film},300}} = 1.3$ mm and $\delta_{Z_{\text{kapton-film},700}} = 0.35$ mm (Table II); consequently, the reflection from the backside of the kapton film will not be differentiated from the reflection from the front side of the kapton film. Besides, the reflection from the backside of the GFRT specimen cannot also be distinguished (it has been explained previously in the Section IV-A). Wherefore, the expected reflections are two; one from the front face of the sample at z $= 0$ mm and the another one from the front face of the kapton film at z $= 0.62$ mm.

Fig. 6(a) and (b) are the reflected spectrum measured by the 300-GHz and 700-GHz imaging systems, respectively, at $x = 35$ mm and $y = 8$ mm. It can be noticed that the 300-GHz reflected spectrum has only a single peak, whereas the 700-GHz reflected spectrum has two peaks. This demonstrates that the reflection from the kapton film can only be recognized by the 700-GHz imaging system. Also, Fig. 6(c) and (d) which represent the *XZ* layer at $y = 8$ mm emphasize this notice, where the yellow dashed line in both figures represents the reflection from the surface at $z = 0$ mm and the black dashed line in Fig. 6(d) points to the reflection from the kapton film.

The reflected amplitude images from the surface (*XY* plane at z $= 0$ mm) measured by both systems can be seen in Fig. 6(e) and (f). In addition, the subsurface layers at $z = 0.6$ mm measured by both systems are presented in Fig. 6(g) and (h).

The presented spectrum in Fig. 6(b) shows that the difference in amplitude between the two peaks is around -3 dB. However,

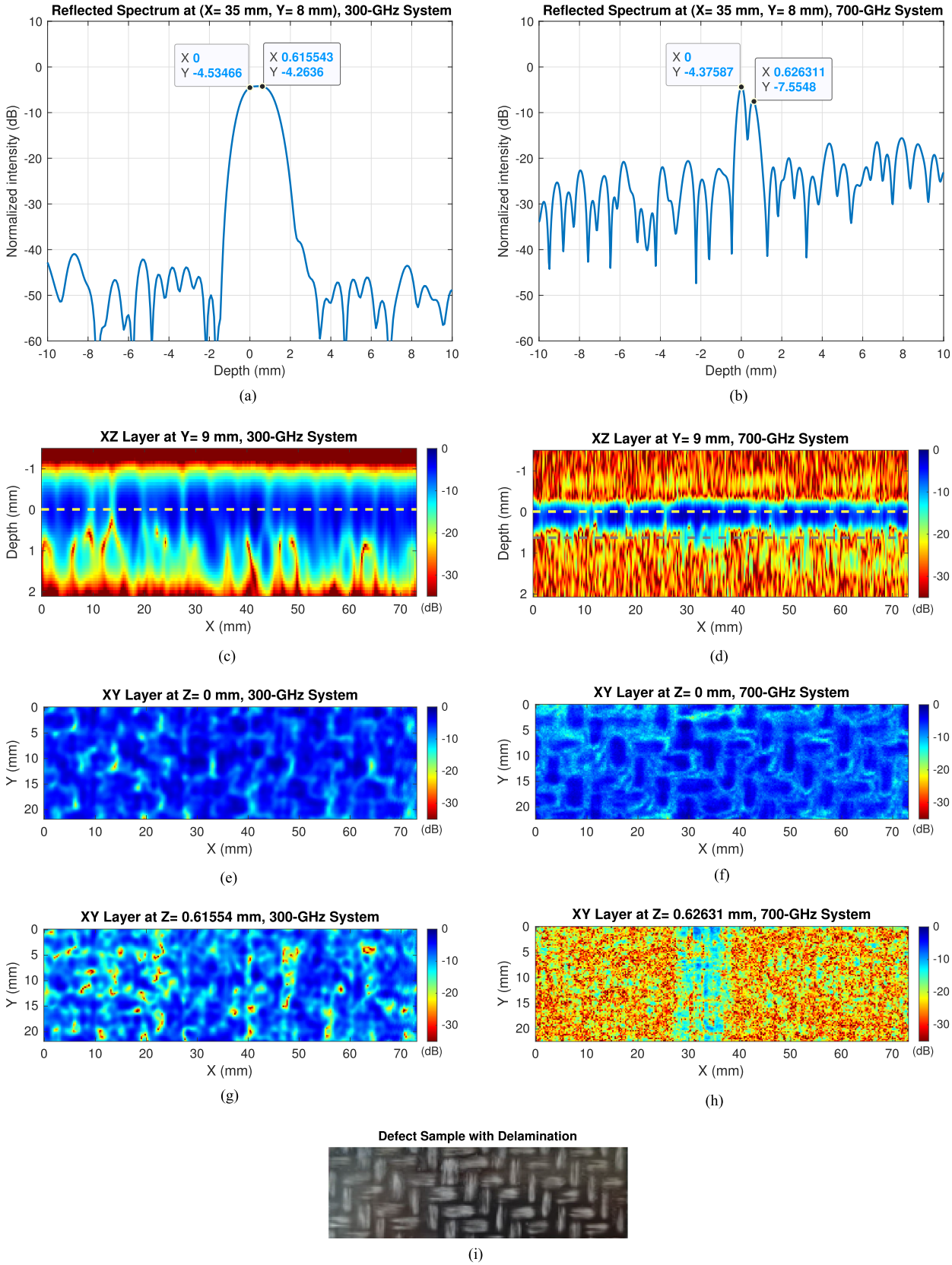

Fig. 6. Comparison of the 300-GHz (left) and 700-GHz (right) imaging systems results measured from the defective sample with a delamination defect. (a) and (b) Reflected spectrum at $x = 35$ mm and $y = 8$ mm. (c) and (d) Depth layer at $y = 9$ mm. The dashed yellow line in both figures denotes to the surface reflection ($z = 0$ mm) and The dashed black line in (d) denotes to the reflection from the kapton film. (e) and (f) Reflected amplitude image of the defective sample surface at $z = 0$ mm. (g) and (h) Reflected amplitude image of the delamination defect. (i) Photograph of the measured defect sample with delamination.

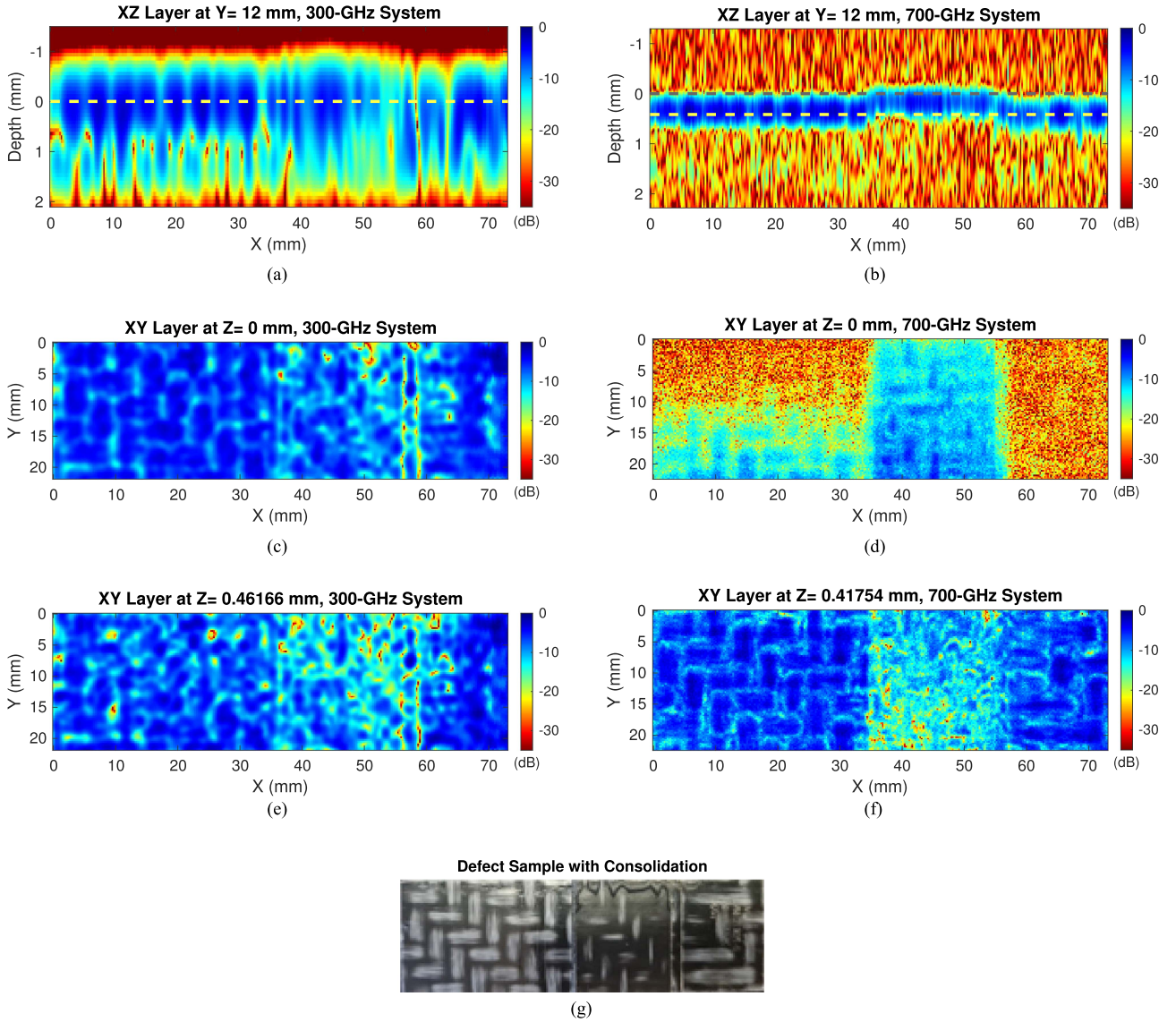

Fig. 7. Comparison of the 300-GHz (left) and 700-GHz (right) imaging systems results measured from the defective sample with a consolidation defect. (a) Depth layer at $y = 12$ mm measured by the 300-GHz imaging system. The dashed yellow line denotes to the reflection from both defective and nondefective areas. (b) Depth layer at $y = 12$ mm measured by the 700-GHz imaging system. The dashed black line denotes to the surface reflection from the defective area. The dashed yellow line denotes to the surface reflection from the nondefective area. (c) Reflected amplitude image of both defective and nondefective areas. (d) Reflected amplitude image of the front face of the defective area measured by the 700-GHz imaging system. (e) Reflected amplitude image at $Z = 0.46$ mm measured by the 300-GHz imaging system. (f) Reflected amplitude image of the front face of the nondefective area measured by the 700-GHz imaging system. (g) Photograph of the measured defect sample with consolidation.

from Fig. 6(h) it can be noticed that the amplitude values in the delamination area varies between -7 to -35 dB. This indicates that not all spectra reflected from the delamination area have two separated peaks because the depth resolution in the air $\delta_{Z_{\text{air},700}} = 0.64$ mm is not always less than the delamination position in Z-direction which changes between 0.4 to 0.7 mm.

It should be noted that the studied sample (artificial delamination defect) is more critical than the nature delamination defect (only air-gap). The main reason for that is the difference in the complex refractive indices between the kapton film and air which will therefore affect the reflection coefficient r_{12} as well as the transmission coefficient t_{12}. However, from (12c) it can be observed that the reflection from the second surface is effected by the reflection coefficient r_{12} which is in the case of GFRT-air $r_{\text{GFRT-air}} = 0.4106 - 0.0105i$ higher than the reflection coefficient in the case of GFRT-kapton film $r_{\text{GFRT-kapton film}} = 0.1333 - 0.0073i$. This leads to lower reflected amplitude from GFRT-kapton film than the reflected one from GFRT-air. As a conclusion, if the THz system can detect the artificial delamination defect, it will surely detect the nature delamination which has the same position in depth and same thickness.

C. Defective Samples: Consolidation Defect

The thicknesses of the nondefective and defective areas of the defective sample with a consolidation defect have been

measured by a digital caliper. The thickness of the defective area is nearly 1.7 mm, while it is roughly 1.3 mm in the nondefective one. As a result, the number of expected reflections from this specimen is three; one from the front face of the defective area at $z = 0$ mm, one from the front face of the nondefective area at $z = 0.4$ mm and a reflection from the rear face of the specimen. However, because the reflection from the backside of the GFRT sample cannot be discriminated, as it has been explained in the Section IV-A, the number of expected reflections is only two. The photograph of the measured defective sample with a consolidation defect can be seen in Fig. 7(g).

The difference in thickness can clearly be seen by looking at the depth layer (*XZ* layer). Fig. 7(a) is the *XZ* layer at $y = 12$ mm measured by the 300-GHz imaging system. It is apparent that the 300-GHz imaging system cannot detect the difference in thickness because the depth resolution of the 300-GHz imaging system in the GFRT composite $\delta_{Z_{\text{GFRT},300}} = 0.692$ mm is higher than the difference in thickness between the nondefective and defective areas 0.4 mm. Fig. 7(c) represents the amplitude image at $z = 0$ mm and Fig. 7(e) presents the subsurface image at $z = 0.46$ mm. Similar to what has been inferred from the Fig. 7(a), the reflection from the surface of the consolidation area and from the nondefective area cannot be separated.

The *XZ* layer data at $y = 12$ mm measured by the 700-GHz imaging system in Fig. 7(b) proves that the difference in thickness can be detected clearly with this system, because the depth resolution of the 700-GHz imaging system in the GFRT laminates $\delta_{Z_{\text{GFRT},700}} = 0.267$ mm is significantly less than the difference in thickness between the nondefective and defective areas 0.4 mm. Fig. 7(d) presents the reflected amplitude image of the front face of the defective area at $z = 0$ mm and Fig. 7(f) shows the reflected amplitude image of the front face of the nondefective area at $z = 0.417$ mm.

V. Conclusion

This article discusses from a simulation and experimental viewpoint the ability of an all-electronic 3-D-THz imaging system to detect hidden defects in a lightweight composite materials with a thickness of 1.5 mm. The bidirectional E-glass fiber reinforced thermoplastic composite material has been inspected with a THz system for the first time in this research. The FMCW technology has been implemented to generate 3-D images. Two THz-FMCW 3-D imaging systems with two different operation frequencies; 277.8 and 616 GHz, have been utilized to inspect the nondefective and defective GFRT specimen. The performance of the two imaging systems has been simulated. In addition, the real measurement results collected from both 3-D imaging systems have been compared. It has been found that the 300-GHz imaging system is not sufficient to detect a hidden defect in a thin material due to the limitation of the depth resolution. However, the use of the 700-GHz imaging system which has a bandwidth three times higher than the bandwidth of the 300-GHz imaging system has improved the depth resolution remarkably. Due to this improvement, such a system can detect delamination defect with a thickness of 125 μm and measure the difference in material thickness which is less than 0.4 mm. In comparison to the THz-TDS system used in [25], our presented 700-GHz imaging system shows similar analysis capabilities (detecting delamination defect with a thickness of 125 μm in different kind of GFRP laminates but with the same thickness of 1.5 mm), but it has better properties. First of all, it is based on all-electronic devices and is a low-power system. It does not need special environmental conditions to work efficiently like the one in [25], where dry air needs to be provided to prevent water vapor absorption. Second, it is less expensive than the THz-TDS system used in [25]. In addition, determining the hidden defect position in depth is much simpler than in the THz-TDS system. Last but not least, it is significantly easier to expand such an electronic system into an MIMO system for real-time in-line inspection in a manufacturing environment.

Acknowledgment

All samples have been produced by Bond-Laminates - a company of the LANXESS Group.

References

[1] D. D. Chung, "Materials for lightweight structures, civil infrastructure, joining and repair," in *Composite Materials: Science and Applications*, London, U.K.: Springer, 2010, pp. 131–156.
[2] D. K. Rajak, D. D. Pagar, R. Kumar, and C. I. Pruncu, "Recent progress of reinforcement materials: A comprehensive overview of composite materials," *J. Materials Res. Technol.*, vol. 8, no. 6, pp. 6354–6374, 2019.
[3] P. U. Jepsen, D. G. Cooke, and M. Koch, "Terahertz spectroscopy and imaging–Modern techniques and applications," *Laser Photon. Rev.*, vol. 5, no. 1, pp. 124–166, 2011.
[4] G. Tripathi, "Application and future of composite materials: A review," *Int. J. Composite Constituent Materials*, vol. 3, no. 2, pp. 6907–6911, 2017.
[5] M. A. Masuelli, "Introduction of fibre-reinforced polymers- polymers and composites: Concepts, properties and processes," in *Fiber Reinforced Polymers-The Technology Applied for Concrete Repair*. Rijeka, Croatia:IntechOpen, 2013.
[6] M. O. Seydibeyoglu, A. K. Mohanty, and M. Misra, *Fiber Technology for Fiber-Reinforced Composites*. Cambridge, U.K.: Woodhead Publishing, 2017.
[7] M. Ö. Seydibeyoğlu, A. Doğru, M. B. Kandemir, and Ö. Aksoy, "Lightweight composite materials in transport structures," in *Lightweight Polymer Composite Structures*. Boca Raton, FL, USA: CRC, 2020, pp. 103–130.
[8] J. Fan and J. Njuguna, "An introduction to lightweight composite materials and their use in transport structures," in *Lightweight Composite Structures in Transport*. New York, NY, USA: Elsevier, 2016, pp. 3–34.
[9] P. Mallick, "Thermoplastics and thermoplastic–matrix composites for lightweight automotive structures," in Materials, Design and Manufacturing for Lightweight Vehicles. New York, NY, USA: Elsevier, 2021, pp. 187–228.
[10] S. N. A. B. Safri, M. Sultan, and M. Jawaid, "Damage analysis of glass fiber reinforced composites," in *Durability and Life Prediction in Biocomposites, Fibre-Reinforced Composites and Hybrid Composites*. New York, NY, USA: Elsevier, 2019, pp. 133–147.
[11] J. Wang, J. Zhang, T. Chang, and H.-L. Cui, "A comparative study of non-destructive evaluation of glass fiber reinforced polymer composites using terahertz, X-ray, and ultrasound imaging," *Int. J. Precis. Eng. Manuf.*, vol. 20, no. 6, pp. 963–972, 2019.
[12] B. Baccouche et al., "Three-dimensional terahertz imaging with sparse multistatic line arrays," *IEEE J. Sel. Topics Quantum Electron.*, vol. 23, no. 4, Jul./Aug. 2017, Art. no. 8501411.
[13] C. Weisenstein, M. Kahl, F. Friederich, and P. H. Bolívar, "Conception and realization of a semiconductor based 240 GHz full 3D mimo imaging system," in *Proc. Terahertz, RF, Millimeter, and Submillimeter-Wave Technol. and Appl. X*, vol. 10103, 2017, Art. no. 101030B.
[14] F. Gumbmann and L.-P. Schmidt, "Millimeter-wave imaging with optimized sparse periodic array for short-range applications," *IEEE Trans. Geosci. Remote Sens.*, vol. 49, no. 10, pp. 3629–3638, Oct. 2011.

[15] R. Heremans, M. Vandewal, and M. Acheroy, "Synthetic aperture imaging extended towards novel THz sensors," in *Proc. IEEE SENSORS*, 2008, pp. 438–441.
[16] N. Schreiner, A. Keil, W. Sauer-Greff, R. Urbansky, and F. Friederich, "Comparison of signal processing algorithms for high-resolution FMCW terahertz thickness measurements," in *Proc. J. Phys. Conf. Ser.*, 2020, Art. no. 012018.
[17] J. Dong, X. Wu, A. Locquet, and D. S. Citrin, "Terahertz superresolution stratigraphic characterization of multilayered structures using sparse deconvolution," *IEEE Trans. THz Sci. Technol.*, vol. 7, no. 3, pp. 260–267, May 2017.
[18] T. M. Wong, M. Kahl, P. H. Bolívar, and A. Kolb, "Computational image enhancement for frequency modulated continuous wave (FMCW) THz image," *J. Infrared Millimeter Terahertz Waves*, vol. 40, no. 7, pp. 775–800, 2019.
[19] M. A. Abou-Khousa, D. L. Simms, S. Kharkovsky, and R. Zoughi, "High-resolution short-range wideband FMCW radar measurements based on music algorithm," in *Proc. IEEE Instrum. Meas. Technol. Conf.*, 2009, pp. 498–501.
[20] E. Zhao, F. Zhang, D. Zhang, and S. Pan, "Three-dimensional multiple signal classification (3D-MUSIC) for super-resolution FMCW radar detection," in *Proc. IEEE MTT-S Int. Wireless Symp.*, 2019, pp. 1–3.
[21] J. Zhang et al., "Nondestructive evaluation of carbon fiber reinforced polymer composites using reflective terahertz imaging," *Sensors*, vol. 16, no. 6, 2016, Art. no. 875.
[22] J. Zhang et al., "Spectroscopic study of terahertz reflection and transmission properties of carbon-fiber-reinforced plastic composites," *Opt. Eng.*, vol. 54, no. 5, 2015, Art. no. 054106.
[23] K.-H. Im et al., "Terahertz wave approach and application on FRP composites," *Adv. Materials Sci. Eng.*, vol. 2013, 2013, Art. no. 563962.
[24] J. Xu et al., "Terahertz imaging and vibro-thermography for impact response in carbon fiber reinforced plastics," *Infrared Phys. Technol.*, vol. 109, 2020, Art. no. 103413.
[25] C.-H. Ryu, S.-H. Park, D.-H. Kim, K.-Y. Jhang, and H.-S. Kim, "Nondestructive evaluation of hidden multi-delamination in a glass-fiber-reinforced plastic composite using terahertz spectroscopy," *Composite Structures*, vol. 156, pp. 338–347, 2016.
[26] D.-H. Kim, C.-H. Ryu, S.-H. Park, and H.-S. Kim, "Nondestructive evaluation of hidden damages in glass fiber reinforced plastic by using the terahertz spectroscopy," *Int. J. Precis. Eng. Manuf. Green Technol.*, vol. 4, no. 2, pp. 211–219, 2017.
[27] C. Stoik, M. Bohn, and J. Blackshire, "Nondestructive evaluation of aircraft composites using reflective terahertz time domain spectroscopy," *NDT E Int.*, vol. 43, no. 2, pp. 106–115, 2010.
[28] H. Richter et al., "Non-destructive testing of glass-fibre reinforced polymers using terahertz spectroscopy," in *Proc. Euro. Conf. Non-Destructive Testing*,2006, pp. 1–8.
[29] J. Wang, J. Zhang, T. Chang, L. Liu, and H.-L. Cui, "Terahertz nondestructive imaging for foreign object detection in glass fibre-reinforced polymer composite panels," *Infrared Phys. Technol.*, vol. 98, pp. 36–44, 2019.
[30] S. Becker, T. Ullmann, and G. Busse, "3D terahertz imaging of hidden defects in oxide fibre reinforced ceramic composites," in *Proc. 4th Int. Symp. NDT Aerosp.*, 2012, pp. 1–6.
[31] A. Bassli et al., "Thz reflectometer for 3D imaging at 100 GHz," in *Proc. IEEE Int. Conf. Wireless Technol. Embedded Intell. Syst.*, 2017, pp. 1–5.
[32] E. Cristofani et al., "Nondestructive testing potential evaluation of a terahertz frequency-modulated continuous-wave imager for composite materials inspection," *Opt. Eng.*, vol. 53, no. 3, 2014, Art. no. 031211.
[33] J. Ding, M. Kahl, O. Loffeld, and P. H. Bolívar, "Thz 3-D image formation using SAR techniques: Simulation, processing and experimental results," *IEEE Trans. THz Sci. Technol.*, vol. 3, no. 5, pp. 606–616, May 2013.
[34] M. Kahl, J. Boecking, B. Engel, and P. H. Bolívar, "3D inspection of fiber-reinforced thermoplastics at THz frequencies," in *Proc. IEEE 44th Int. Conf. Infrared Millimeter Terahertz Waves*, 2019, pp. 1–2.
[35] R. Hussung et al., "Aspects of signal processing for multistatic terahertz imaging systems," in *Proc. IEEE 46th Int. Conf. Infrared Millimeter Terahertz Waves*, 2021, pp. 1–2.
[36] A. Souliman et al., "High-bandwidth FMCW THz imaging in the 499-733 GHz range for defect detection in glass fiber reinforced thermoplastics," in *Proc. IEEE 47th Int. Conf. Infrared Millimeter Terahertz Waves*, 2022, pp. 1–2.
[37] H. A. Maddah, "Polypropylene as a promising plastic: A review," *Amer. J. Polym. Sci.*, vol. 6, no. 1, pp. 1–11, 2016.
[38] H. Ning et al., "A review of long fibre thermoplastic (LFT) composites," *Int. Materials Rev.*, vol. 65, no. 3, pp. 164–188, 2020.
[39] J. Shi, M. Mizuno, L. Bao, and C. Zhu, "A facile molding method of continuous fiber-reinforced thermoplastic composites and its mechanical property," *Polymers*, vol. 14, no. 5, 2022, Art. no. 947.
[40] S. Epple and C. Bonten, "Production of continuous fiber thermoplastic composites by in-situ pultrusion," in *Proc. AIP Conf. Proc.*, 2014, pp. 454–457.
[41] Y. Tan, X. Wang, and D. Wu, "Preparation, microstructures, and properties of long-glass-fiber-reinforced thermoplastic composites based on polycarbonate/poly (butylene terephthalate) alloys," *J. Reinforced Plastics Composites*, vol. 34, no. 21, pp. 1804–1820, 2015.
[42] M. Wisnom, "The role of delamination in failure of fibre-reinforced composites," *Philos. Trans. Roy. Soc. A: Math. Phys. Eng. Sci.*, vol. 370, no. 1965, pp. 1850–1870, 2012.
[43] N. Mohan, S. Kulkarni, and A. Ramachandra, "Delamination analysis in drilling process of glass fiber reinforced plastic (GFRP) composite materials," *J. Materials Process. Technol.*, vol. 186, no. 1/3, pp. 265–271, 2007.
[44] P. Rakesh et al., "Delamination in fiber reinforced plastics: A finite element approach," *Engineering*, vol. 3, no. 5, 2011, Art. no. 549.
[45] K. B. Cooper et al., "THz imaging radar for standoff personnel screening," *IEEE Trans. THz Sci. Technol.*, vol. 1, no. 1, pp. 169–182, Sep. 2011.
[46] K. B. Cooper et al., "Using FMCW Doppler radar to detect targets up to the maximum unambiguous range," *IEEE Geosci. Remote Sens. Lett.*, vol. 14, no. 3, pp. 339–343, Mar. 2017.
[47] A. Poole, "Advanced sounding: 1 the FMCW alternative," *Radio Sci.*, vol. 20, no. 6, pp. 1609–1616, 1985.
[48] A. G. Stove, "Linear FMCW radar techniques," *IEE Proc. F-Radar Signal Process.*, vol. 139, no. 5, pp. 343–350, 1992.
[49] Y. Zhou et al., "High-precision terahertz frequency modulated continuous wave imaging method using continuous wavelet transform," *Opt. Eng.*, vol. 57, no. 2, 2018, Art. no. 023108.
[50] S. Gu et al., "Compressed sensing for THz FMCW radar 3D imaging," *Complexity*, vol. 2021, 2021, Art. no. 5576782.
[51] N. Schreiner, B. Baccouche, W. Sauer-Greff, R. Urbansky, and F. Friederich, "High-resolution FMCW millimeter-wave and terahertz thickness measurements," in *Proc. IEEE 47th Eur. Microw. Conf.*, 2017, pp. 1187–1190.
[52] C. Sun et al., "All-electronic terahertz 3-D imaging system based on FMCW," in *Proc. IEEE 46th Int. Conf. Infrared Millimeter Terahertz Waves*, 2021, pp. 1–2.
[53] F. Ellrich et al., "Terahertz quality inspection for automotive and aviation industries," *J. Infrared MillimeterTerahertz Waves*, vol. 41, no. 4, pp. 470–489, 2020.
[54] Y.-S. Son, H.-K. Sung, and S. W. Heo, "Automotive frequency modulated continuous wave radar interference reduction using per-vehicle chirp sequences," *Sensors*, vol. 18, no. 9, 2018, Art. no. 2831.
[55] I.-M. Lee et al., "Frequency modulation based continuous-wave terahertz homodyne system," *Opt. Exp.*, vol. 23, no. 2, pp. 846–858, 2015.
[56] J. Zheng, *Optical Frequency-Modulated Continuous-Wave (FMCW) Interferometry*, vol. 107. Berlin, Germany: Springer, 2005.
[57] E. Cristofani, A. Brook, M. Vandewal, C. Matheis, and J. Jonuscheit, "Assessment of 3D signal and image processing using FMCW THz signals," in *Proc. 5th Int. Symp. Optronics Defense Secur.*, 2012, pp. 1–12.
[58] L. Duvillaret, F. Garet, and J.-L. Coutaz, "A reliable method for extraction of material parameters in terahertz time-domain spectroscopy," *IEEE J. Sel. Topics Quantum Electron.*, vol. 2, no. 3, pp. 739–746, Sep. 1996.
[59] X.-F. Navick et al., "Fabrication of ultra-low radioactivity detector holders for Edelweiss-II," *Nucl. Instrum. Methods Phys. Res. Sect. A Accel. Spectrometers Detectors Assoc. Equip.*, vol. 520, no. 1/3, pp. 189–192, 2004.

Aya Souliman received the B.Sc. degree in mechatronics engineering from the University of Aleppo, Aleppo, Syria, in 2012, and the M.Sc. degree in mechatronics from the University of Siegen, Germany, in 2018.

She was a Research Assistant at the Mechatronics Engineering Department, Faculty of Electrical and Electronic engineering, University of Aleppo, from 2013 to 2015. Since 2019, she has been a Research Associates with the Institute for High Frequency and Quantum Electronics, University of Siegen. Her research interests include 3-D-THz imaging and deep learning.

Matthias Kahl received the diploma degree in electrical engineering from the University of Siegen, Germany, in 2009.

He is currently a Researcher with the Institute for High Frequency and Quantum Electronics, University of Siegen. His research interest includes THz technology and image reconstruction.

Daniel Stock received the diploma degree in electrical engineering and the Ph.D. (Dr.-Ing.) degree in development of model-based methods for the determination of material parameters in the THz-range from the University of Siegen, Germany, in 2011 and 2018, respectively. His thesis was on THz material parameter determination by model-based extraction methods.

Since then, he has been a Researcher with the Institute of High Frequency and Quantum Electronics, University of Siegen. His research interests include broadband terahertz material characterization, especially the analysis of thin, layered structures, and its applications in industrial settings.

Michael Möller received the Ph.D. degree in multiscale methods for polyhedral regularizations and applications in high dimensional imaging from the University of Münster, Münster, Germany, in 2012.

He is currently the head of the Computer Vision Group, University of Siegen, Siegen, Germany. His research interests include combinations of model-based and learning-based techniques in imaging and vision along with efficient optimization algorithms to solve the underlying high dimensional minimization problems.

Bernd Engel received the Ph.D. degree in process strategy for internal high-pressure forming from the University of Darmstadt, Darmstadt, Germany, in 1995.

Since 2003, he has been head of the Chair of Forming Technology, University of Siegen, Siegen, Germany. From 2008 to 2009, he was Dean of the Department of Mechanical Engineering, University of Siegen. Since 2001, he has been a Scientific Director of the Automotive Center Südwestfalen, Attendorn, Germany. His research interests include manufacturing processes of bending, hydroforming, and deep drawing.

Peter Haring Bolívar received the Ph.D. degree in influence of the Coulomb interaction on the coherent and incoherent electronic dynamics in modern optoelectronic materials from the RWTH Aachen, Aachen, Germany.

From 1997 to 2001, he was head of ultrahigh-frequency research with the Institute of Semiconductor Electronics, RWTH Aachen, where he was Head of Research, from 2001 to 2004. Since 2004, he is head of the Institute for High Frequency and Quantum Electronic, University of Siegen, Siegen, Germany, where he became the Vice-Rector for Research of this University, in 2008. He holds eight patents, five book contributions, and over 70 peer-review publications. His research interests include optoelectronics, ultrafast science, ultrahigh frequency devices, optical data storage and nanotechnology.

Dr. Bolívar was the recipient of the Friedrich Wilhelm price of the RWTH Aachen.